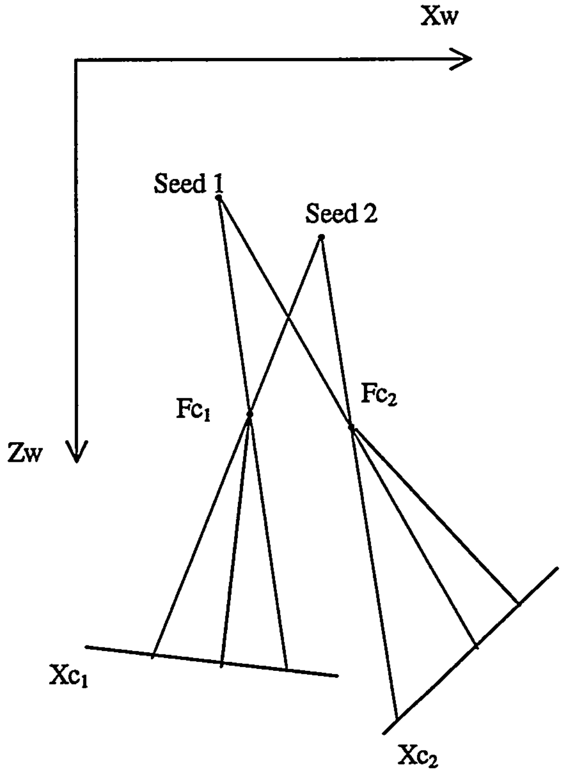

Figure 3.2 Simple model of particle determination.

3.2.2. Theory for Tracking Programs

Just as in two-dimensional PIV (see Ch. 2), two methods have been developed to obtain the displacement of multiple particles between flow images. They are the cross-correlation tracking (CCT) algorithm and the multi-frame particle tracking (MFT) algorithm. These two methods are used in the PST3D and TP3D programs, respectively (see Appendices for details).

The 3D cross-correlation tracking (CCT) algorithm is identical to the 2D CCT algorithm except that comparison volumes, rather than areas, are used. The particle velocity is found by determining the correspondence between particles in the comparison volumes of the two frames. Every particle belongs to a characteristic group that has a specific 3D local distribution pattern in the first space frame and multiple candidate patterns in the second frame. Each second frame candidate's comparison volume is shifted over the first frame comparison volume such that the original particle's center is positioned over the candidate particle's center. The particle in the first frame corresponds to the particle in the second image that maintains the most similar pattern within the comparison volume, providing that the local pattern of the distributed particles changes little within the time that the original images were taken. This method is particularly useful when only two sequential frames are available, and the MFT method cannot be performed.

The CCT algorithm correlates between two frames of data. A search volume is formed in the second frame, centered on the location of the original particle in the first frame. The size of this volume is determined by estimating the maximum possible movement for particles between frames. Each Frame 2 particle in this volume is a candidate for being the original particle as moved by the flow. A comparison volume is then created around each candidate, encompassing at least ten other particles in Frame 2. A comparison volume of the same size is created in Frame 1, centered on the original Frame 1 particle. The two volumes are then compared by shifting the center of the candidate particle over the center of the original particle. This comparison is represented by the correlation coefficient, C_{ij}, which measures the overlap of the particles in the two volumes. A C_{ij} value of 1 indicates a perfect correspondence between two volumes; the closer the value is to 1, the more likely that it is the correct particle match. A C_{ij} value of 1 is only possible if each spot is the same size in both comparison volumes, and each spot is centered in the same point when shifted to overlap the two volumes. The correlation coefficient is calculated just as in the 2D algorithm.

The 3D MFT algorithm is identical to the 2D version, except that search volumes are used in place of search areas. The sequential space frames obtained by particle determination contain the information necessary for the three-dimensional tracking scheme. The MFT routine tracks particles through four frames directly, and then it combines the four frame tracks to indirectly track through all the frames available. Several possible tracks exist for each particle in the first interrogation volume. The search volume in the second frame for a particle starting in the first frame is a sphere of radius, R1, determined by a rough estimate of the maximum velocity of the flow field. The search volumes in the third and fourth frames have their radius, R2, determined by a rough estimate of the maximum acceleration of the flow field. The center of each search volume in frame 3 is found by projecting out along the straight line, L_{1-2}, of a possible track for each particle found in the search volume of frame 2. For each particle found in the search volume of frame 3, the center of a search volume in frame 4 is determined by using the length of the track from frame 2 to 3, L_{2-3}, and the angles created by the track from frame 1 to 3, θ_{1-3} and Φ_{1-3}. This results in several different possible tracks for each particle in frame one, the best of which is used as the actual track for that particle, as determined by the lowest sigma value. If different tracks originating in the same frame share a particle, then the one with the highest sigma value is disposed of as incorrect.

3.3 3D Validation

3.3.1. Synthetic Data

To verify the ability of these two tracking algorithms to track particle movement in three dimensions, two types of tests were conducted. The first test was with synthetic data, and the second with experimental data. To produce the three-dimensional synthetic data, a standard flow was required to create sets of particles at known positions and move them from frame to frame. Simulated inviscid flow around a sphere and simulated flow to a drain were used for this purpose.

Exact analytical solutions were used to move the simulated tracer particles. The tracking method was then performed using these frames of data to produce particle tracks. Comparisons were made between the tracks produced by the algorithms and the known particle tracks.

By comparing the tracks created by the tracking algorithms to the original synthetic tracks, the tracking algorithms can be evaluated (Henderson, 1994). Each algorithm was evaluated with two factors, yield and reliability. The yield is the number of tracks found divided by the number of tracks produced, while the reliability is the number of correct tracks divided by the number of tracks found. By multiplying the two factors together, the number of correct tracks per generated track is obtained. For the synthetic flow around a sphere, the CCT code has a higher yield but a lower reliability at high velocities than the MFT code. Based on synthetic drain flow, the CCT generally has a higher yield but at the cost of lower reliability. Analysis was also performed based on the number of tracks, but it did not show a change in the performance of the codes until more than 5000 tracks per frame were analyzed.

The second validation was performed by examining particle motion on the surface of a spinning disk. For both two-dimensional (flat) and three-dimensional (tilted) motions, the PIV algorithms were shown to work well.

3.3.2. Three-Dimensional Convection Experiment Set-Up

The description of the magma simulant flow chamber experiment was included in the previous chapter for the two-dimensional PIV set-up. No changes were made to the chamber except to lower the constant-temperature cooling plate and cylinder to 10°C and the heater plate to 30°C.

Figure 3.1 shows the basic three-dimensional PIV set-up. Whereas a laser light source was used to illuminate the particles in a plane for 2D (planar) PIV, an overhead projector was used as a light source to provide an easily controllable volume of light for 3D PIV. Calibration points within the chamber were measured by capturing images of crossing calibration laser beams. These calibration lasers were 10 mW diode lasers (670 nm wavelength), whose beams could clearly be seen in the corn syrup. Pictures of the illuminated particles were captured using an array of three CCD cameras (Pulnix TM745). These pictures were directly captured by three EPIX frame grabber boards (4MEG video Model 10) and were saved as binary files for analysis on a 486/66 PC.

3.3.3. Results and Discussion of Three-Dimensional Experiments

The data obtained in the 3D experiment consisted of very sparse, unreliable vector fields. This was due to a number of experimental difficulties, including unanticipated strong refractive index gradients, which made absolute calibration impossible. In addition, diurnally induced temperature drifts and material degradation (carmelization) after prolonged heating contributed to the difficulties in acquiring accurate data.

Thermal refraction was the biggest cause of problems. It caused errors in calibrating the cameras which then carried over to spot combination. With these calibration errors, the cross-correlation tracking routine could not function properly, as shown by an average C_{ij} value of approximately 0.1 for the 3D experiments. By comparison, the 2D thermal convection experiments had average C_{ij} values > 0.3, and the 2D channel flow average C_{ij} values were even higher.

3.4 3D PIV Validation Computations

The computational fluid dynamics code FIDAP (Fluid Dynamics International, 1993) was used to simulate the three-dimensional natural-convection experiment discussed above. Figure 3.5 shows a schematic diagram of the experiment. The geometry under examination is a cubical box (2L = 56 cm side), within which a closed cylinder (7.6 cm diameter, 28 cm height) has been end-mounted to the center of the top side. The top side of the box and cylinder are water-cooled, and a flush-mounted heater strip (56 cm length, 14 cm width) is centered on the bottom side of the box. All the other boundaries are insulated. The interior of this apparatus is completely filled with 42/43 corn syrup, which has been used by other investigators (e.g., Chu and Hickox, 1990) as a magma simulant because of its highly temperature-dependent viscosity. The conditions examined are cold and hot temperatures of $T_C = 8.8°\text{C}$ and $T_H = 31.7°\text{C}$, which correspond to a cold-to-hot viscosity ratio of 37, and cold Prandtl and Rayleigh numbers (based on the box half width) of $Pr = 6.7\times10^6$ and $Ra = 2.2\times10^4$, respectively, where $Ra = \rho^2 cg\beta(T_H - T_C)L^3/\mu k$. The temperature-dependent material properties of 42/43 corn syrup are given below, with the viscosity μ in Poise, the thermal conductivity k in W/m·K, the specific heat c in J/g·K, the density ρ in g/cm^3, and the coefficient of thermal expansion β in K^{-1}, where the temperature T is in °C.

$$\mu = a_0 \exp[a_1 \exp(-T/a_2)],\ a_0 = 0.2412,\ a_1 = 12.5867,\ a_2 = 55.7805$$

$$k = b_0 + b_1 T,\ b_0 = 0.3724,\ b_1 = 3.034\times10^{-4}$$

$$c = c_0 + c_1 T + c_2 T^2,\ c_0 = 2.2005,\ c_1 = 3.9532\times10^{-3},\ c_2 = -6.7883\times10^{-6}$$

$$\rho = \rho_0[1 - \beta(T - T_0)],\ \rho_0 = 1.4255,\ \beta = 4.1218\times10^{-4},\ T_0 = 10$$

Prior to simulation using FIDAP, this problem is formulated in nondimensional form. The following scalings are employed:

Table 2.2.1 Nondimensionalization of properties

Quantity	Symbol	At $T_C = 8.8°\text{C}$	At $T_H = 31.7°\text{C}$	Scaled Value
Box Half Width	L	0.28 m	0.28 m	1
Density	ρ	1430.7 kg/m^3	1444.2 kg/m^3	$1/Pr$ (cold, hot)

Table 2.2.1 Nondimensionalization of properties

Quantity	Symbol	At $T_C = 8.8$°C	At $T_H = 31.7$°C	Scaled Value
Viscosity	μ	1124.4 kg/m·s	30.1 kg/m·s	$1/Ra^{1/2}$ (cold)
Thermal Expansion Cf.	β	4.1238×10^{-4}/K	4.1238×10^{-4}/K	Pr (cold, hot)
Specific Heat	c	2234.8 J/kg·K	2319.0 J/kg·K	Pr (cold)
Thermal Conductivity	k	0.3751 W/m·K	0.3820 W/m·K	$1/Ra^{1/2}$ (cold)
Gravity	g	9.81 m/s^2	9.81 m/s^2	1

Table 2.2.2 Nondimensionalization of variables

Quantity	Symbol	Scaled Form	Numerical Value
Position	$\mathbf{x}$	$\mathbf{x}/L$	$L = 0.28$ m
Velocity	$\mathbf{u}$	$\mathbf{u}/U\ ,\ U = Ra^{1/2}(k/\rho c L)$	$U = 6.21\times10^{-5}$ m/s
Pressure	p	$p/P\ ,\ P = \rho g \beta (T_H - T_C) L$	$P = 37.1$ Pa
Temperature	T	$(T - T_C)/(T_H - T_C)$	$T_C = 8.8$°C, $T_H = 31.7$°C

Table 2.2.3 Dimensionless parameters

Parameter	Symbol	Value
Prandtl Number	$Pr = \mu c/k$	6.7×10^6 (cold)
Rayleigh Number	$Ra = \rho^2 c g \beta (T_H - T_C) L^3/\mu k$	2.2×10^4 (cold)
Viscosity Ratio	μ_C/μ_H	37
Reynolds Number	$Re = \rho U L/\mu = Ra^{1/2}/Pr$	2.2×10^{-5} (cold)
Peclet Number	$Pe = \rho c U L/k = Ra^{1/2}$	148 (cold)

Several observations can be made based on the above scaling. First, the Reynolds number is very low. Thus, inertial effects such as “jetting” are nonexistent: the fluid motion is determined by a force balance between hydrostatic pressure, buoyancy, and viscous effects. Second, the Peclet number is rather high at cold conditions and is higher still at hot conditions, so the thermal boundary layers are thin. Since the flow is driven solely by buoyancy, inaccurate determination of the boundary layers would produce inaccurate heat transfer results, inaccurate buoyant forces, and inaccurate velocity values, even in the interior of the flow, so good resolution of the boundary layers is essential to obtaining an accurate flow solution. This combination of thin boundary layers and three-dimensionality makes this a computationally intense problem.

The computational fluid dynamics code FIDAP is used to determine the velocity and temperature fields for the natural-convection flow problem outlined above and shown in Figure 3.5. Due to the symmetries in the problem, the computational domain consists of one-fourth of the physical domain. The flow is assumed to be steady, and the penalty method with a 10^{-5} penalty parameter is used to enforce incompressibility. The solution is computed on two different meshes (see Figure 3.6), where the more refined mesh has 1.5 times the nodal density of the more coarse mesh in all three coordinate directions. Comparisons of the results on these meshes indicates that a reasonable degree of grid independence is achieved (see Figure 3.7).

Figures 3.8-3.14 show contour plots of the field variables, and Figure 3.15 shows selected streamlines. Velocity components and temperature are seen to have thin boundary layers, as expected. The maximum speed is approximately 2.9 (corresponding to 0.2 mm/s), which indicates that the scaling used is physically sensible. The dominant contribution to the pressure is hydrostatic. The temperature is relatively uniform throughout the interior of the fluid (outside of the plume and the boundary layers), as would be expected for this high Peclet number. The streamlines in Figure 3.15 show a marked resemblance to flow-visualization pictures, shown in Figure 3.16. However, the fluid beneath the cylinder is moving downward toward the heater strip, contrary to initial expectations based on the two-dimensional simulations (without a cylinder) of Chu and Hickox (1990) and Hickox and Chu (1991) (see Torczynski et al. (1995)) After approaching the middle of the heater strip, the fluid subsequently moves out toward the sides of the box along the heater strip and up along the wall at the wall-heater junction (see also Figures 2.19 through 2.22 for 2D results).

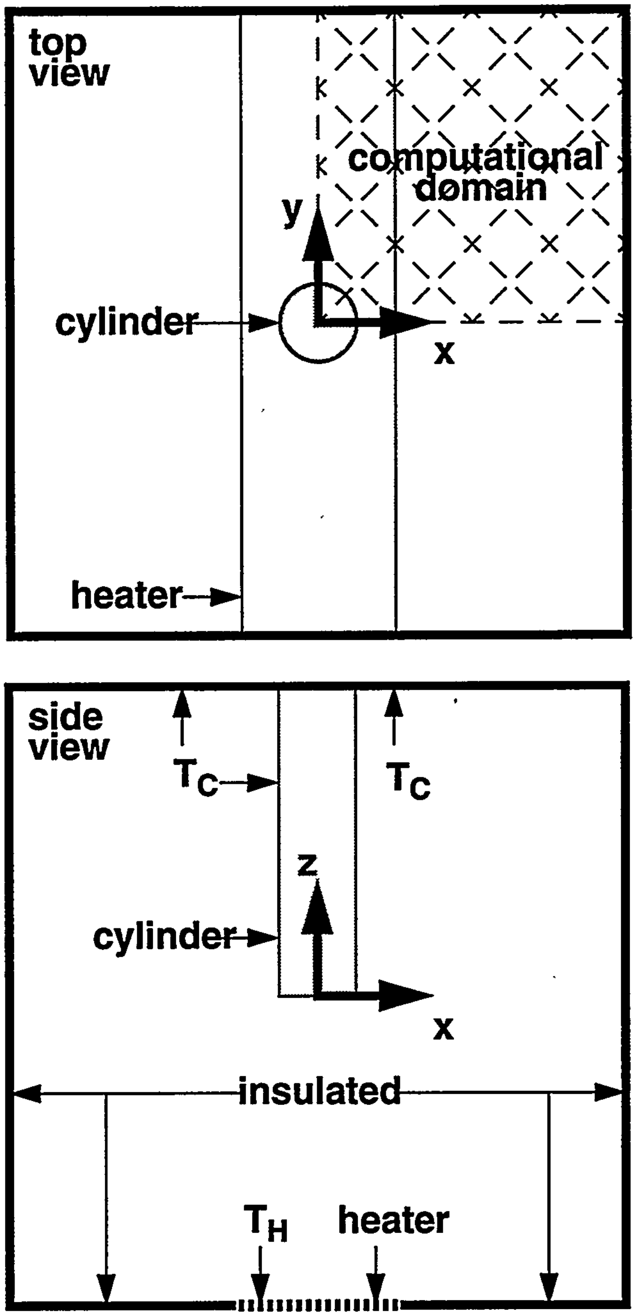

Figure 3.3 Schematic diagrams showing different views of the geometry.

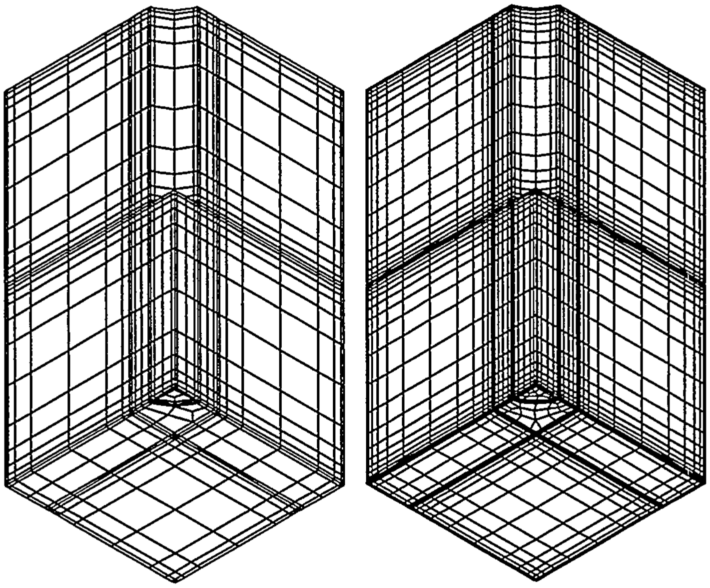

Figure 3.4 Left, coarse mesh. Right, refined mesh. Tri-linear brick elements.

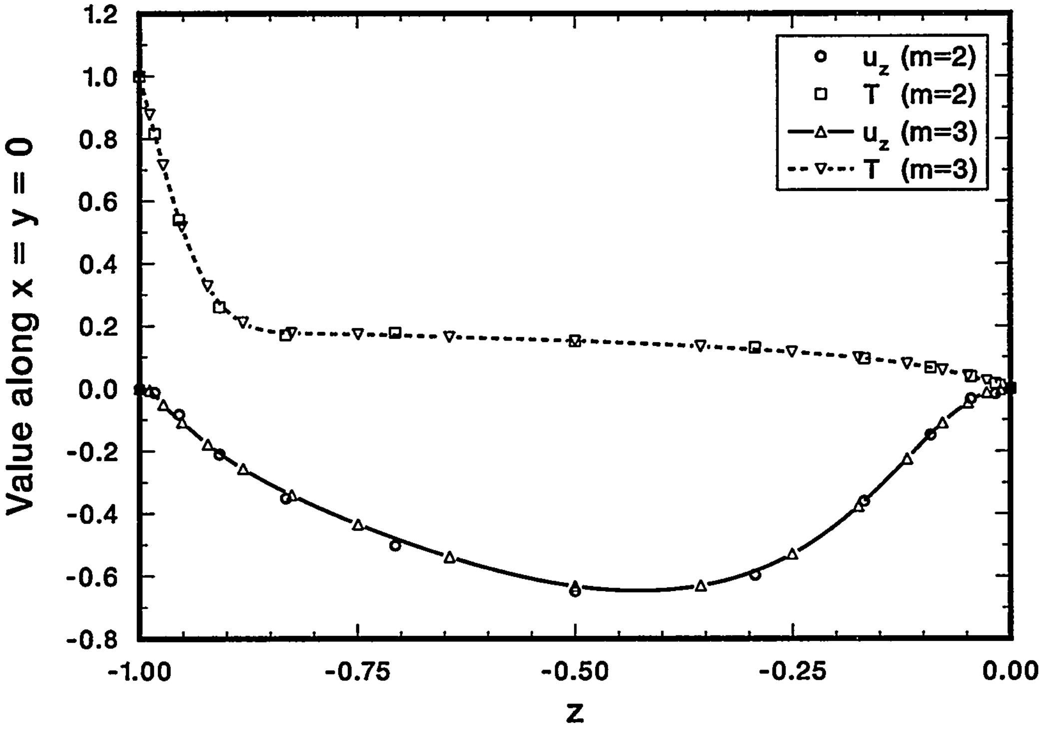

Figure 3.5 Effect of mesh on u_z and T along $x = y = 0$ (below the cylinder on its axis).

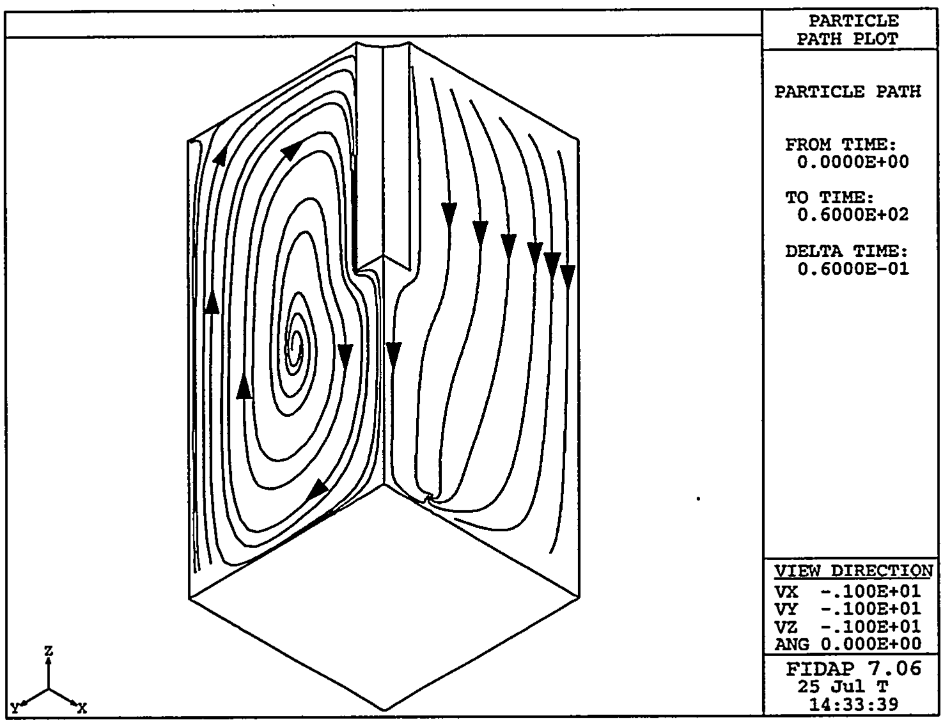

Figure 3.6 Selected streamlines on symmetry planes.

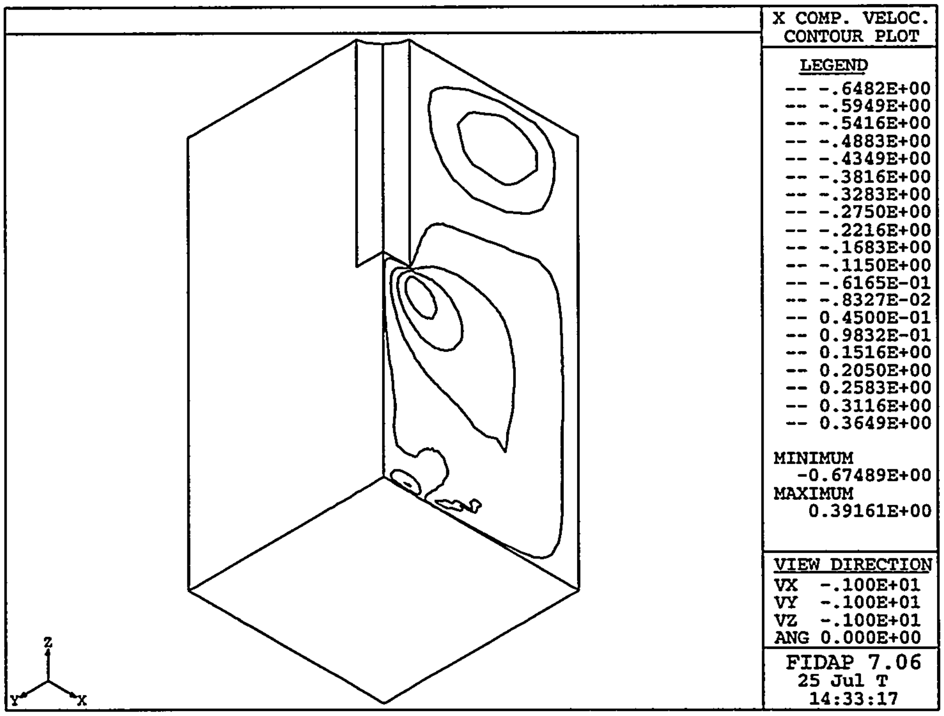

Figure 3.7 Contour plot of u_x.

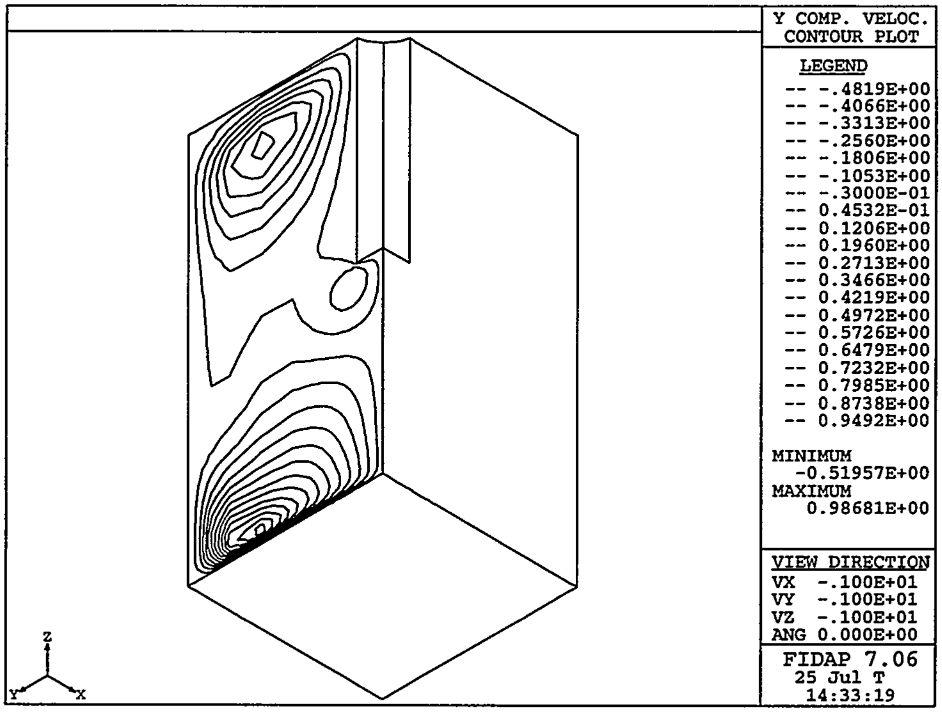

Figure 3.8 Contour plot of u_y.

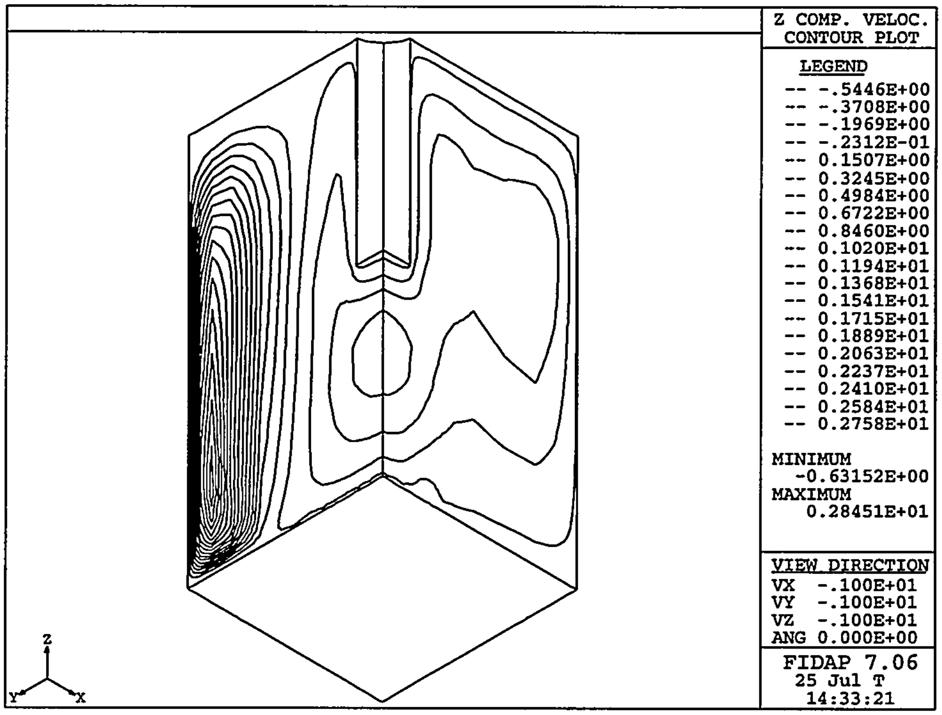

Figure 3.9 Contour plot of u_z.

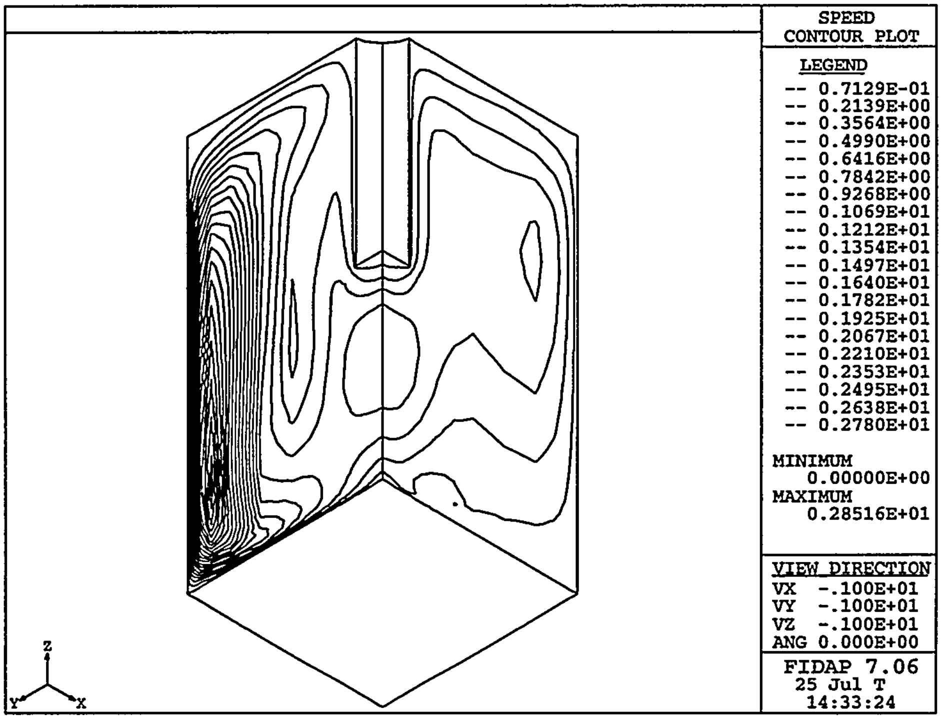

Figure 3.10 Contour plot of speed v.

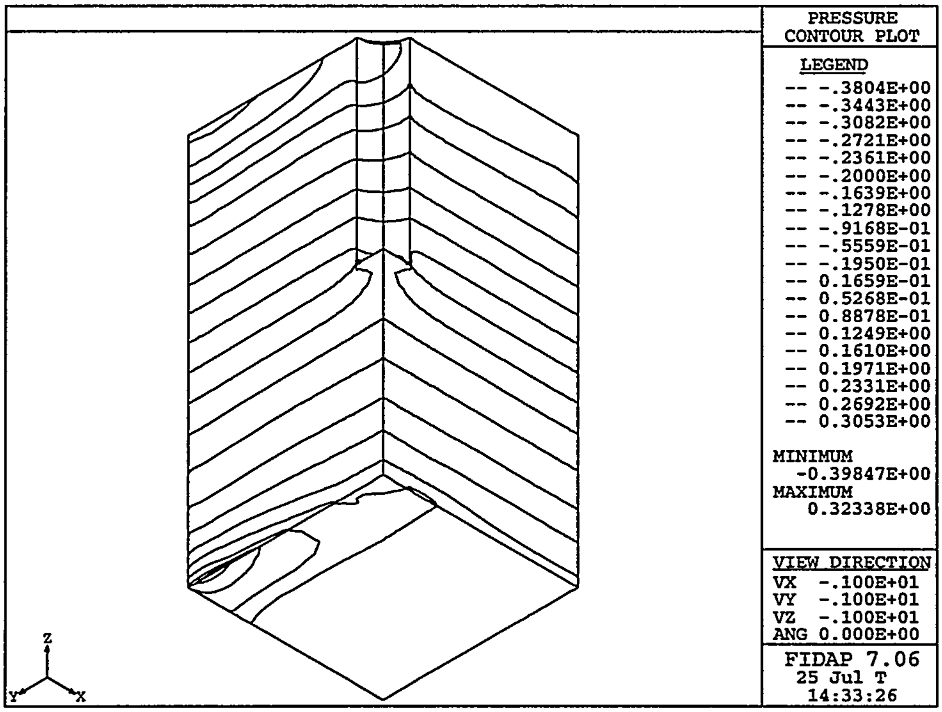

Figure 3.11 Contour plot of pressure p.

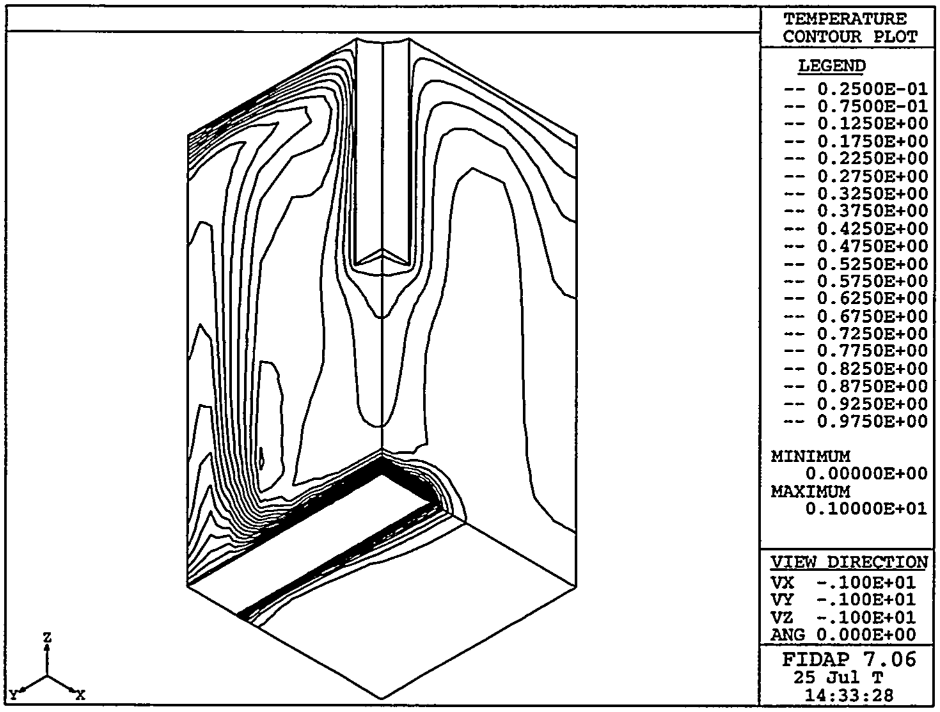

Figure 3.12 Contour plot of temperature T.

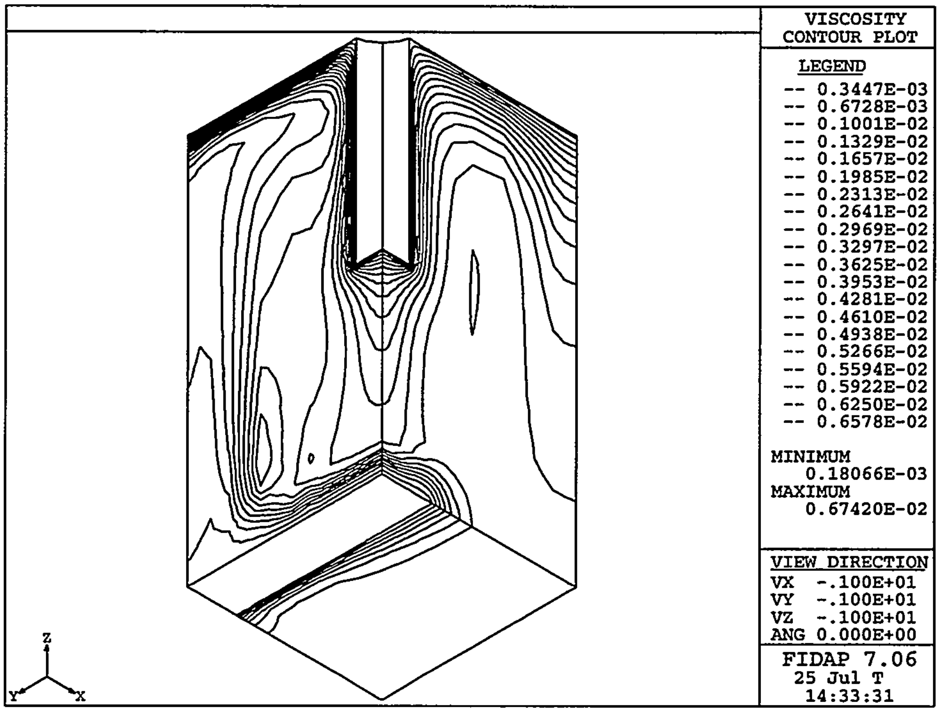

Figure 3.13 Contour plot of viscosity μ.

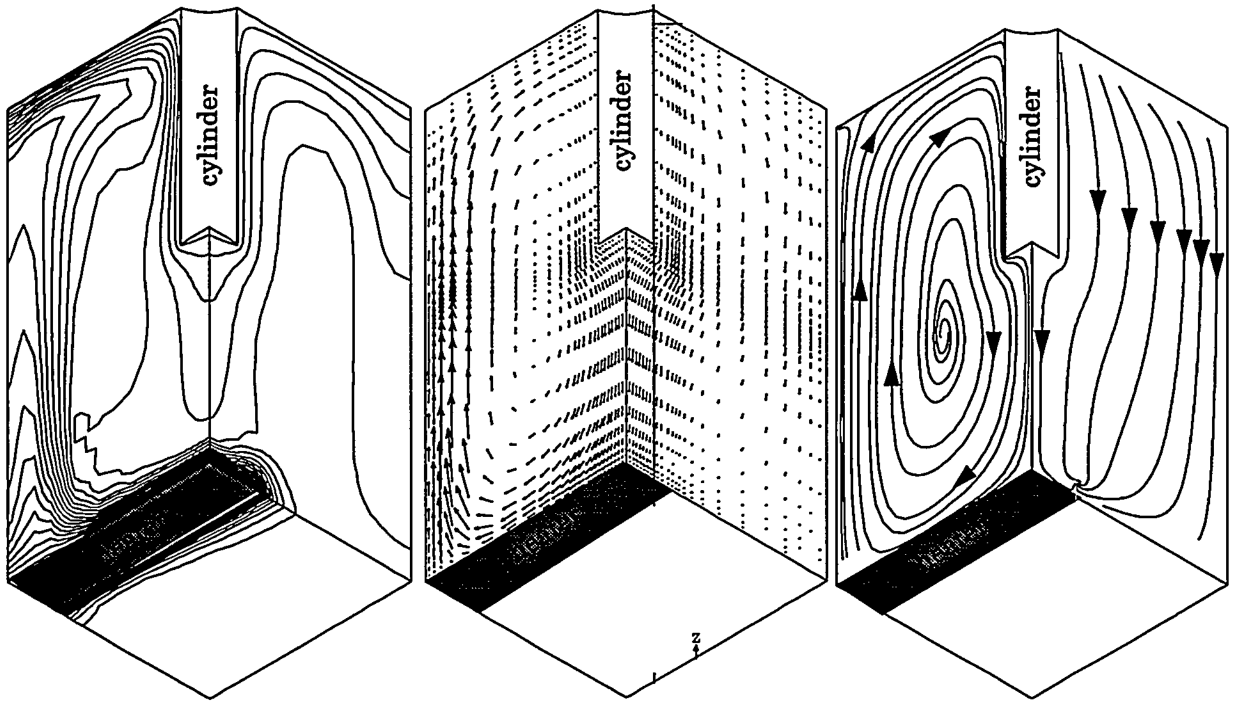

Figure 3.14 Computational results: left, temperature contours; center, velocity vectors; right, selected streamlines on symmetry planes.

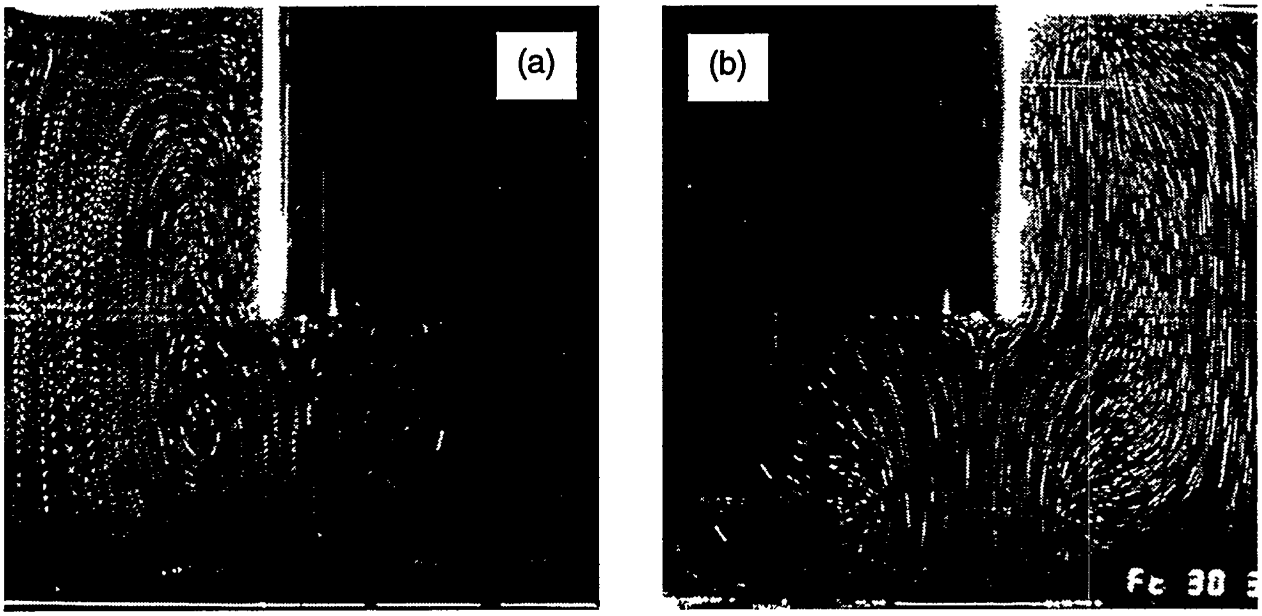

Figure 3.15 Laser light sheet flow-visualization photographs: (a) slice through cylinder along heater; (b) slice through cylinder across heater.